NJC

Accepted Manuscript

This is an *Accepted Manuscript*, which has been through the Royal Society of Chemistry peer review process and has been accepted for publication.

Accepted Manuscripts are published online shortly after acceptance, before technical editing, formatting and proof reading. Using this free service, authors can make their results available to the community, in citable form, before we publish the edited article. We will replace this *Accepted Manuscript* with the edited and formatted *Advance Article* as soon as it is available.

You can find more information about *Accepted Manuscripts* in the **Information for Authors**.

Please note that technical editing may introduce minor changes to the text and/or graphics, which may alter content. The journal's standard **Terms & Conditions** and the **Ethical guidelines** still apply. In no event shall the Royal Society of Chemistry be held responsible for any errors or omissions in this *Accepted Manuscript* or any consequences arising from the use of any information it contains.

www.rsc.org/njc

NJC

ARTICLE

A thin empty-shell bismuth tungstate hierarchical structure constructed by acid sculpture effect and improved visible-light photocatalytic activity

Chunmei Li,[a] Gang Chen,[a*] Jingxue Sun,[a*] Yujie Feng,[b] Hongjun Dong,[a,c] Zhonghui Han,[a] Yidong Hu[a] and Chade Lv[a]

A thin empty-shell bismuth tungstate hierarchical structure is constructed using acid sculpture effect without any templates or surfactants by a facile hydrothermal process, which is composed of ultrathin nanosheets (~14.0 nm). It results in the large specific surface area and abundant pores through its inside and outside of the thin empty-shell, which shortens transport distance of organic molecules and provides the plenty of reaction active sites for improving photocatalytic activity. The thin empty-shell bismuth tungstate hierarchical structure can more effectively remove colored RhB and colorless phenol in aqueous solutions relative to the typical bismuth tungstate. The possible evolved mechanism of the thin empty-shell hierarchical structure and the photocatalytic reaction mechanism are discussed in detail.

Introduction

During the past decades, semiconductor photocatalysts have been regarded as one of most efficient and economical alternative to remove organic pollutants for solving environmental pollution problems.[1-3] How to improve the photocatalytic activity of extant photocatalysts is still an important work because exploiting the new high-efficiency photocatalysts is very difficult. It is well known that there are close correlations between the physical/chemical properties of semiconductor photocatalysts and their morphology, size and structure.[4-6] Therefore, the much increase interests concentrate on improving photocatalytic activity by means of designing and preparing hierarchical photocatalytic materials with unique nano/micro-structure units.[7-8] As a kind of promising photocatalytic material, Bi_2WO_6 can construct the diverse hierarchical architectures to improve photocatalytic activity owing to its superior intrinsic physical and chemical properties.[9-11]

To date, many considerable efforts have focused on preparing Bi_2WO_6 micro- and nano-crystals with various morphologies to enhance their photocatalytic activity, such as nanoparticles,[12] nanoplates,[13] microsphaeric,[14] tyre-/helix-like,[15] clew-like,[16] porous thin films,[17] hollow sphere[18] and so on. Among these nanostructures, the hierarchical hollow architecture exhibits some unique advantages owing to their low density, large surface area and good permeation features.[19-22] In recent years, some different methods have been devoted to preparing

Bi_2WO_6 hollow architecture. For instance, Li et al. have reported that Bi_2WO_6 hollow microspheres were synthesized using polystyrene particles as the template via a hydrothermal process.[23] Wu et al. reported the synthesis of Bi_2WO_6 hollow nanospheres with a sacrificial templates approach by converting the reaction medium from aqueous solution to water and ethanol mixed solvent.[24] In addition, Huang and co-workers also reported Bi_2WO_6 hollow microspheres prepared by an anion exchange method.[25] The Bi_2WO_6 hollow microspheres prepared by these methods all improve the photocatalytic performance to various degrees. However, one inevitable problem is that constructing them involves hard template, soft template or other additives serving as structure-directing reagent, which may suffer from high cost, difficult purify and tedious preparation process as well as even may prevent them from large-scale production. The other is that they seem to rarely consider the influence of structural features on the photocatalytic activity of Bi_2WO_6 hollow architectures. We know that the ultrathin sheet units can produce a synergistic effect of accommodating the volume swing and facilitate charge carriers transport and separation.[7] In addition, the thin shell thickness is in favour of entrance of organic molecules into the inner of the photocatalysts. Therefore, provided that we exploit a simple method to synthesize the thin empty-shell Bi_2WO_6 hierarchical structure constructed by ultrathin nanosheets, it will make an important progress for improving photocatalytic activity of Bi_2WO_6.

Herein, in this paper, we fabricate the thin empty-shell Bi_2WO_6 hierarchical structure composed of ultrathin nanosheets by means of acid sculpture effect. It exhibits the more superior photodegradation activity for removing coloured RhB dye and colourless phenol in aqueous solutions relative to the typical Bi_2WO_6 sample. We also propose the possible crystal growth mechanism revealing the formation process of the thin empty-shell Bi_2WO_6 hierarchical structure and photocatalytic reaction mechanism.

Experimental

Preparation and Characterizations

All the raw materials were purchased from commercial sources and used without further purification. In a typical synthesis, firstly, 0.3 mL nitric acid solution was added into the bismuth nitrate ($Bi(NO_3)_3·5H_2O$, 1 mmol) solution to make it dissolve completely. Following, sodium tungstate ($Na_2WO_4·2H_2O$, 0.5 mmol) was added into the above solution drop by drop under vigorous magnetic stirring for 2h, and then the suspension was transferred into a 25 mL Teflon lined stainless steel autoclave to execute hydrothermal process at 160 °C. After cooling down to the room temperature, the sample was collected by centrifugation and washed with deionized water and ethanol in turn. The thin empty-shell Bi_2WO_6 hierarchical structure was finally obtained by drying at 80 °C for 20h (TES-Bi_2WO_6). Simultaneously, the traditional Bi_2WO_6 sample is also prepared by a solid-state reaction (SSR-Bi_2WO_6) according to ref 26 serving as a contrast.

The phase of as-prepared Bi_2WO_6 sample was characterized by powder X-ray diffractometer (XRD, RigakuD/max-2000) equipped with a Cu-Kα radiation at a scanning rate of 5° min^{-1} in the 2θ range of 10-90°. X-ray tube voltage and current were set at 45 kV and 50 mA, respectively. The morphologies of samples were characterized by field-emission scanning electron microscopy (FESEM, FEI QUANTA 200F). Transmission electron microscopy (TEM) and high-resolution TEM (HR-TEM) of samples were also carried out on FEI Tecnai G2 S-Twin and they are operated at 300 kV. X-ray photoelectron spectroscopy (XPS) analysis was measured on an American electronics physical system (HI5700ESCA) with X-ray photoelectron spectroscope using Al Kα (1486.6 eV) monochromatic X-ray radiation. The peak positions were corrected against the contaminated carbon C 1s peak (284.6 eV). The UV-vis diffuse reflectance spectra (DRS) of the samples were recorded on a UV-vis spectrophotometer (PG, TU-1901) with $BaSO_4$ as the background between 250 nm and 600 nm at room temperature. The nitrogen adsorption and desorption isotherm, pore size distribution and specific surface area were measured using an AUTOSORB-1 surface area and pore size analyzer at 77K.

Photocatalytic and Photoelectrochemical Measurements.

The photocatalytic activities were evaluated by the degradation of coloured RhB and colourless phenol aqueous solution under visible light irradiation in quartz photochemical reactor. A 300 W Xenon lamp (Trusttech PLS-SXE 300, Beijing) covered with a UV filter (λ>400 nm) was used as a light source. The photodegradation was performed at room temperature as follows: the RhB (phenol) solution (10 mg L^{-1}, 100 mL) containing 0.05g Bi_2WO_6 was carried out about 5 min ultrasonic process and kept in dark for 55 min to achieve adsorption-desorption equilibrium between RhB (phenol) and photocatalysts under continuous magnetic stirring, then adding 0.1ml H_2O_2 to reactor before irradiation. Every 10 min of time intervals, 3 mL mixture was collected from the suspension liquid, followed by centrifuged at 10^4 rpm for 3 min. The absorbance of RhB (phenol) solution was analysed by measuring the absorbance at λ = 554 nm (273 nm) with the UV-visible spectrophotometer (PG, TU-1901).

The photoelectrochemical properties were measured in the CHI604C electrochemical working station employing a standard three-compartment cell under visible light assembled by a 300 W Xe lamp. The Bi_2WO_6 samples coated at FTO glass, a kind of Ag/AgCl electrode, a piece of Pt sheet, and 0.01 M sodium carbonate were used as the working electrode, reference electrode, counter-electrode and electrolyte, respectively.

Results and discussion

The phase compositions of the as-prepared thin empty-shell Bi_2WO_6 hierarchical structure (TES-Bi_2WO_6) are identified by XRD. The typical XRD pattern in Fig. 1a is well-indexed as orthorhombic Bi_2WO_6 (JCPDS card No.39-0256), and no other impurity phase diffraction peaks are detected. It demonstrates that the identical crystalline phase Bi_2WO_6 products are obtained. Furthermore, the resulting sharp and intense diffraction peaks also indicate the as-prepared TES-Bi_2WO_6 has high-crystallinity. The morphologies of TES-Bi_2WO_6 are confirmed by FESEM. As shown in Fig. 1b, the FESEM image exhibits largescale monodispersed flower-like architectures
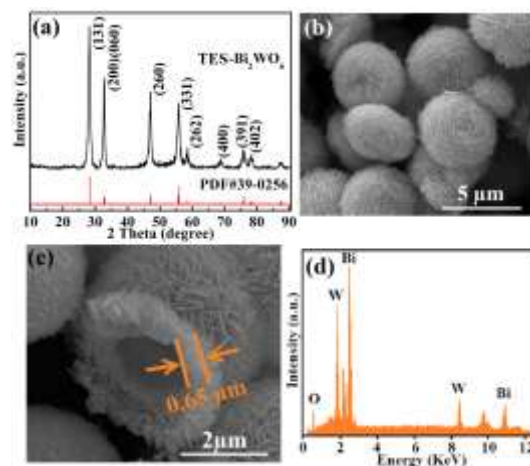

Fig. 1 XRD pattern (a), SEM images (b, c) and the EDS spectrum (d) of the thin empty-shell Bi_2WO_6 hierarchical structure.

with diameter of ~4 μm and they are composed of two dimensional nanosheets when hydrothermal reaction reaches to 22 h. The aggregation pattern of these nanosheets can generate numerous pores on nanoscale, which may act as the small molecule transport paths in favor of molecules diffusing into the inner of thin empty-shell. Importantly, the thin empty-shell hierarchical structure feature is testified by the broken architecture formed at hydrothermal reaction 30h. From the FESEM image of the broken architecture in Fig. 1c, it shows the thin empty-shell architecture feature with the wall thickness of ~0.65 μm, which can shorten the transport distance of organic molecules from outside of empty-shell to inner. In addition, the EDS spectrum of TES-Bi_2WO_6 in Fig. 1d exhibits that the sample contains Bi, O and W elements and the atomic ratio of Bi to W to O is close to 2:1:6 of stoichiometric proportion in Bi_2WO_6.

The detailed microstructure characteristics of TES-Bi_2WO_6 sample are further investigated by TEM. Fig. 2a-b show the bright and dark field TEM images of multiple and individual Bi_2WO_6 microspheres, respectively. Both of them display an obvious brightness difference between the edge and center, further confirming the thin empty-shell hierarchical structure feature of Bi_2WO_6 architecture. The individual TES-Bi_2WO_6 is also investigated by high-magnification TEM images (Fig. 2c-d). The image recorded at the edge of individual architecture further exhibits that it is actually built by 2D ultrathin nanosheets with the thicknesses of ~14.0 nm. In order to further confirm the thickness of nanosheet, the TEM measurement is carried out with different angles (Fig. S1), demonstrating the thickness of nanosheet is indeed about 14.0 nm. The ultrathin feature of these nanosheets can also shorten transfer distance of perpendicular to nanosheet planes to improve the transfer and separation of electron-hole pairs. Moreover, the symmetric diffraction spots in SAED pattern performed on the individual ultrathin nanosheet reveals that a perfect Bi_2WO_6 single crystal is achieved, where the marked diffraction spot is indexed as the (131) atomic planes of orthorhombic Bi_2WO_6 (Fig. 2e). In addition, the lattice parameters of TES-Bi_2WO_6 are identified by HRTEM (Fig. 2f). The interplanar spacing of ultrathin nanosheet is 0.315 nm, which agrees well with the (131) crystal
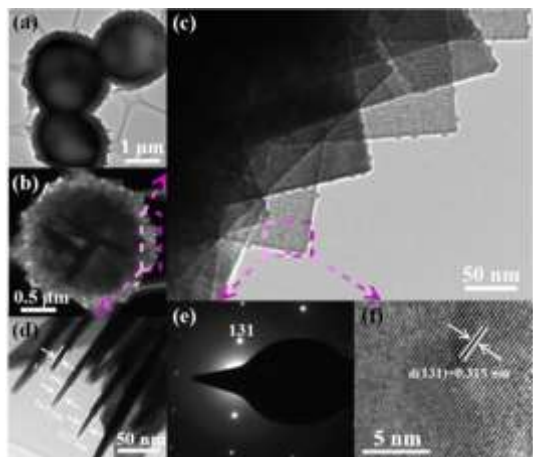
Fig. 2 TEM images (a-d), SAED pattern (e) and HRTEM image (f) of TES-Bi_2WO_6.

planes of orthorhombic Bi_2WO_6.[27] It is in agreement with the result of SAED pattern. All above prove that the thin empty-shell Bi_2WO_6 hierarchical structure is successfully constructed by the ultrathin nanosheets
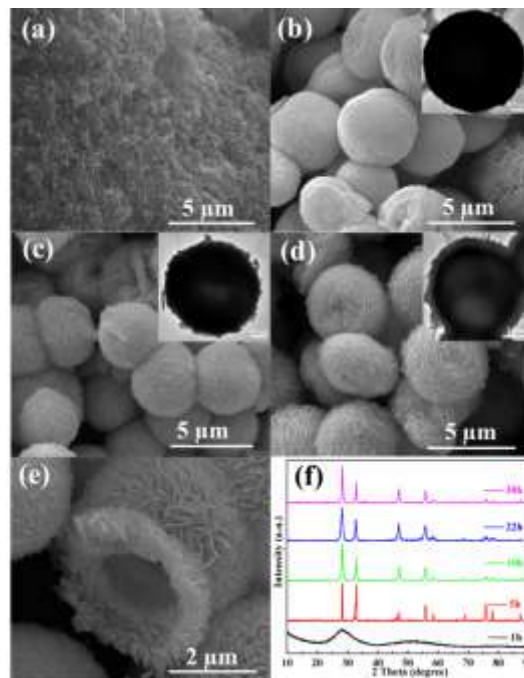

Fig. 3 FESEM and TEM images of morphology evolution for TES-Bi_2WO_6 with reaction time variation, (a) 1 h (b) 5 h, (c) 10h, (d) 22 h and (e) 30 h as well as the corresponding XRD patterns (f).

In order to ascertain the evolved mechanism of the ultrathin nanosheet forming thin empty-shell Bi_2WO_6 hierarchical structure, the FESEM and TEM images of time-dependent morphology evolution for the hierarchical thin empty-shell Bi_2WO_6 architecture and the corresponding XRD patterns are performed (Fig. 3). From the FESEM in Fig. 4a and the widened XRD diffraction peaks in Fig. 3f, the plenty of Bi_2WO_6 nanoparticles with low crystallinity are generated after 1 h hydrothermal reaction. When the reaction is carried out for 5 h, as the FESEM and TEM images displayed in Fig. 3b and XRD pattern in Fig. 3f, the irregular Bi_2WO_6 architectures with rough surface and high crystallinity are formed via an "initial crystallization" process.[28] In this process, the irregular Bi_2WO_6 architectures are solid (TEM image in the insert of Fig. 3b). Proceeding reaction to 10 h, the irregular Bi_2WO_6 architectures composed with small nanosheets are obtained and the hollowing interiors appear around the center of the irregular architectures in this stage (Fig. 3c). Further prolonging the reaction time to 22 h, the well-defined hierarchical thin empty-shell architecture is constructed by the nanosheets, which can be clearly observed from the FESEM and TEM images in Fig. 3d. Upon gradual evolution of the Bi_2WO_6 architectures, the perfect architecture is broken after the reaction of 30 h (Fig. 3e), which demonstrates its thin empty-shell architecture feature.

Meanwhile, we should point out all of the Bi_2WO_6 samples obtained at the reaction of 5h, 10h, 22h and 30h exhibit high crystallinity (Fig 3f).

Based on the above experimental results, the possible construction mechanism of thin empty-shell Bi_2WO_6 hierarchical structure composed of ultrathin nanosheets is shown in Scheme 1. It mainly involves nucleation, self-assembly, acid sculpture and Ostwald ripening process. In the primary stage, the low-crystallinity Bi_2WO_6 nanoparticles are generated by simple precipitation reaction (step 1). Then a mass of low-crystallinity Bi_2WO_6 nanoparticles self-aggregate into orbicular solid spheres for minimizing the total surface energy (step 2).[29] As the reaction proceeding, the aggregated Bi_2WO_6 nanoparticles start further crystallization in the internal and outside surfaces of sphere. It prefers to grow into two dimensionally nanosheet structure through the dissolution-recrystallization process (step 3) owing to the own layered crystal feature of Bi_2WO_6.[30] Compared with the outside surface, the inner crystallites have the higher solubility and surface energy due to the initial high supersaturation.[31] Thus, the inner crystallites dissolve and migrate out to reduce their surface energy under the acid sculpture, which can provide the driving force for the Ostwald ripening and then result in interior void space (step 4). With prolonging reaction time, the inner void space largens slowly and the thin empty-shell architecture is formed after further ripening process (step 5). We have to emphasize that, the acid sculpture effect play a key role for the formation of ultrathin nanosheets and thin shell in the whole incessant growth of the hierarchical Bi_2WO_6 architecture. It has been proved by the in-situ nanosheet formation on the architecture surface in each stage as revealed by FESEM and TEM images.
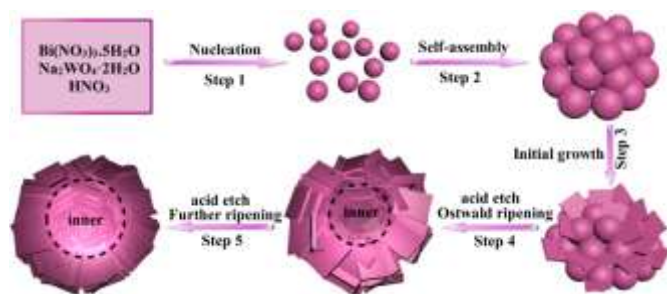
Scheme 1. The schematic diagram of crystal growth mechanism of TES-Bi_2WO_6 sample

The chemical composition and surface valence states of the TES-Bi_2WO_6 sample are analyzed using XPS technique. As shown in Fig. 4a, it shows that the obvious binding energy peaks attribute to W 4f, Bi 4f, W 4d, Bi 4d, O 1s, Bi 4p and O auger state, respectively, which indicates that the as-obtained sample is composed of Bi, W, and O elements. The banding energy peaks at 158.8 eV and 164.1 eV in Fig. 4b derive from Bi^{3+} $4f_{7/2}$ and $4f_{5/2}$ states, respectively.[32] In addition, Fig. 4c exhibits two banding energy peaks at 35.0 eV and 37.1 eV, which belong to W^{6+} $4f_{7/2}$ and $4f_{5/2}$ states, respectively.[33] Furthermore, the binding energy peak at 530.0 eV in Fig. 4d

belongs to O 1s state.[34] As a result, the obtained sample is recognized as pure Bi_2WO_6 based on the results of XRD and XPS analysis.
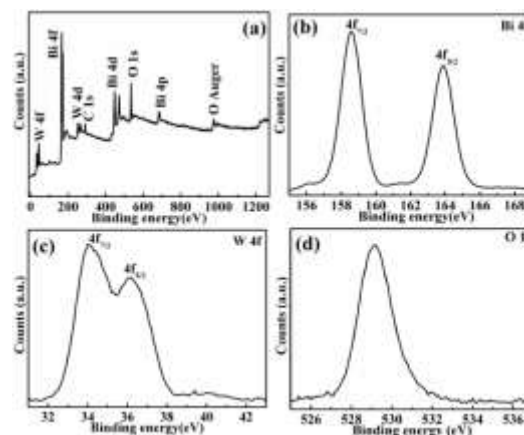

Fig. 4 Survey (a) and high-resolution XPS spectra of Bi 4f (b), W 4f (c) and O 1s (d) for TES-Bi_2WO_6 sample.

The UV-vis DRS spectra are measured to evaluate light absorption property of TES-Bi_2WO_6 and SSR-Bi_2WO_6 samples using as comparison (Fig. 5). The steep absorption edge shapes of them indicate that the intense absorptions are not due to the transition from the impurity level but band-gap transition.[35] Both of them show the superior visible-light absorption ability. The absorption edge of the TES-Bi_2WO_6 is 459 nm, which shows a little redshift compared with that of SSR-Bi_2WO_6. It indicates the visible-light response wavelength region is broadened. In addition, the band gaps of them are further estimated according to the research method of crystal semiconductor reported by M. A. Butler.[36] Bi_2WO_6 is a typical indirect band gap semiconductor.[37] Using plots of $(\alpha h v)^{1/2}$ versus hv (insert), we achieve band gap values of 2.55 eV and 2.61 eV for TES-Bi_2WO_6 and SSR-Bi_2WO_6, respectively. The narrow forbidden bandwidth implies the electrons are more easily excited from the VB to CB for the TES-Bi_2WO_6.
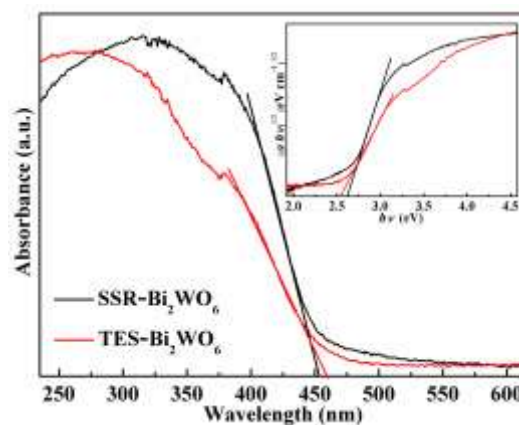

Fig. 5 UV-vis DRS and plots of $(\alpha h v)^{1/2}$ versus hv (insert) of SSR-Bi_2WO_6 and TES-Bi_2WO_6 samples.

The photocatalytic activities of TES-Bi_2WO_6 and SSR-Bi_2WO_6 are evaluated by degrading the coloured RhB dye
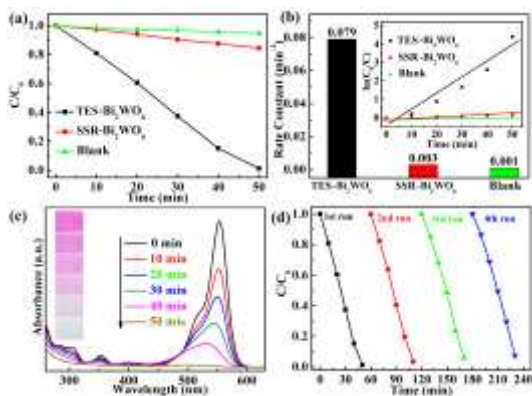

Fig. 6 Dynamic curves of photodegradation (a), plots of $\ln(C_0/C)$ versus time (insert of b) and rate constant k (b) for RhB solutions over SSR-Bi_2WO_6 and TES-Bi_2WO_6, absorbance (c) and color (the insert of c) variations of RhB solution, cycle runs of photodegradation RhB solution (d) over TES-Bi_2WO_6 sample.

under visible light irradiation. As shown in Fig. 6a, the TES-Bi_2WO_6 displays the higher photodegraded activity than that of SSR-Bi_2WO_6. The removal rate of RhB is close to 100% after photocatalytic reaction of 50 min over the TES-Bi_2WO_6 sample. Furthermore, the kinetic curves of RhB photodegradation are approximated as a pseudo-first-order process.[38] The plots of $\ln(C_0/C)$ vs time are shown in the insert of Fig. 6b. Employing the fitting results of these plots, the removal rate constant k (Fig. 6b) of RhB over the TES-Bi_2WO_6 sample is 0.079 min^{-1}, which is much higher than that of typical SSR-Bi_2WO_6 (0.003 min^{-1}) and blank without photocatalyst (0.001 min^{-1}), respectively. Fig. 6c shows the absorbance and color variation of RhB solutions, in which the absorbance of RhB solution at both ultraviolet and visible region all disappear after reacting 50 min and the maximum absorption wavelength of RhB solutions is not shifting. It indirectly demonstrates that the benzene or heterocyclic rings may be destroyed completely and decomposed into small organic/inorganic molecules or/and ions products.[39-40] Furthermore, considering the reusability and stability of photocatalysts are significance in the practical application, the circle experiments of RhB degradation are carried out under visible light irradiation. The photodegradation ability of TES-Bi_2WO_6 sample has not significantly loss after four recycles (Fig. 6d), indicating that it possesses ideal stability and durability. The photodegradation of colourless phenol as target molecule is also carried out to further verify the photocatalytic activity of TES-Bi_2WO_6 and SSR-Bi_2WO_6 samples. Fig. 7a shows that the phenol in the aqueous solution is completely decomposed after 250 min under visible light irradiation over the TES-Bi_2WO_6 sample. Moreover, the removal rate constant k also reaches to 0.012 min^{-1} (Fig. 7b), which is six times as much as that of SSR-Bi_2WO_6 sample (0.002 min^{-1}). All above demonstrate that the thin empty-shell Bi_2WO_6 hierarchical structure can serve as a kind of outstanding photocatalytic material.

The superior photocatalytic activity of thin empty-shell Bi_2WO_6 hierarchical structure mainly results from the high separation efficiency of charge carriers. As is well-known, the
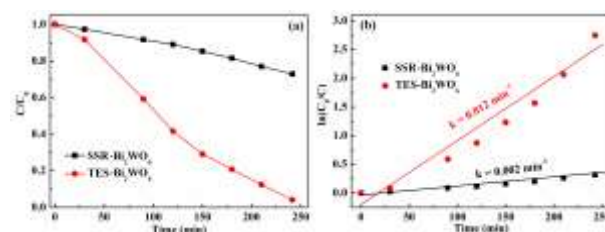

Fig. 7 Dynamic curves of photodegradation (a) and plots of $\ln(C_0/C)$ versus time (b) for phenol solutions over SSR-Bi_2WO_6 and TES-Bi_2WO_6 samples.

intense photocurrent response suggests the high charge collection efficiency on the electrode surface, and indirectly evidences the high separated efficiency of electron-hole pairs.[41-43] Fig. 8 shows that the stronger dark current of TES-Bi_2WO_6 film electrodes only in the external electric field illustrates it has good electron-hole separation ability and conductive capability itself, which contributes to electron-hole transfer inside the sample. Moreover, the SSR-Bi_2WO_6 and TES-Bi_2WO_6 film electrodes are quickly generating photocurrent under visible light, respectively, in which the TES-Bi_2WO_6 sample produces the more intense photocurrent response in comparison with that of SSR-Bi_2WO_6. It indicates that the separated efficiency and the lifetime of the photogenerated charge carriers are improved over the TES-Bi_2WO_6 sample film electrode. The above results imply that the thin empty-shell Bi_2WO_6 hierarchical structure can efficiently separate photogenerated electron-hole pairs and reduce their recombination rate, thus improving photocatalytic activity.
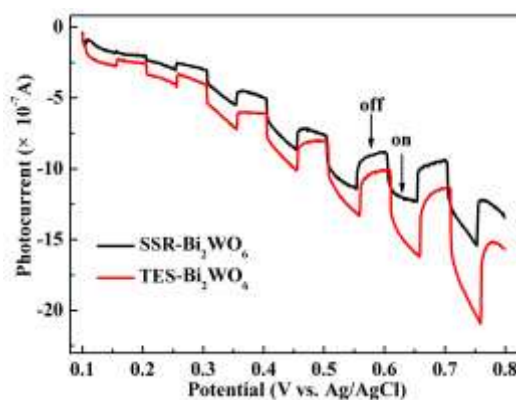

Fig. 8 Photocurrent responses of SSR-Bi_2WO_6 and TES-Bi_2WO_6 samples.

In addition, the specific surface area and pore diameter distribution are also important parameters influencing photocatalytic activity. The nitrogen adsorption-desorption isotherms and Barrett-Joyner-Halenda (BJH) pore diameter distribution measurements over the TES-Bi_2WO_6 sample are carried out (Fig. 9). According to the IUPAC classifications, the isotherm of TES-Bi_2WO_6 belongs to type IV with a H3

hysteresis loop appeared in the range of 0.5-1.0 (P/P$_0$), attesting the presence of mesopores.[44] It is also determined by the corresponding pore diameter distributions (the inset in Fig. 9), which shows dominant peaks in the mesoporous range (2-50 nm) and another peaks at ~100 nm. It confirms the presence of macropores (>50 nm) besides mesoporus,[45, 46] which can be attributed to the empty-shell structure feature and nanosheet interspaces of the hierarchical Bi$_2$WO$_6$ architecture. In addition, the Brunauer-Emmett-Teller (BET) surface area of TES-Bi$_2$WO$_6$ (17.85 m^2 g^{-1}) is larger than that of SSR-Bi$_2$WO$_6$ (0.89 m^2 g^{-1}). The larger surface area and more abundant pore distribution are also important reasons for enhancing photocatalytic activity.
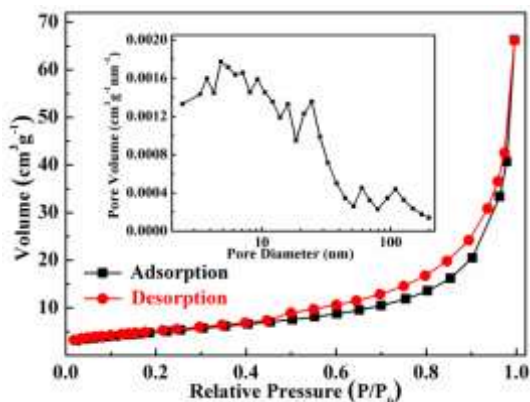

Fig. 9 N$_2$ adsorption-desorption curves and pore diameter distributions (insert) of TES-Bi$_2$WO$_6$ sample.

The possible photocatalytic reaction mechanism is shown in Scheme 2. When the thin empty-shell Bi$_2$WO$_6$ hierarchical structure exposed to the visible light, the multiple reflections can be produced within the interior cavity of sample to improve its light harvesting capacity.[47] Furthermore, the RhB/phenol molecules can easily diffuse into the interior of TES-Bi$_2$WO$_6$ by passing through the abundant pore channels. Therefore, the photocatalytic reactions are able to simultaneously take place on the internal and external surface of the TES-Bi$_2$WO$_6$ sample. As our previous report,[48] a mass of electrons-hole pairs are generated under the visible light irradiation, then separate and transfer to the sample surface. A little part of electrons are captured by the dissolved oxygen in water to produce superoxide radicals ($\cdot$O$_2^-$) and a mass of electrons react with H$_2$O$_2$ molecules to generate hydroxyl radicals ($\cdot$OH). Superoxide radicals, hydroxyl radicals and holes all can degrade RhB/phenol molecules. In addition, H$_2$O$_2$ also serves as an efficient electron scavenger, which is in favor of the charge carriers' separation for improving the photocatalytic activity.
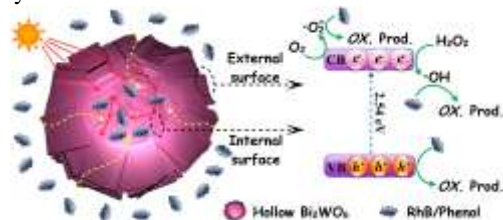
Scheme 2. Possible photocatalytic mechanism of TES-Bi$_2$WO$_6$ sample.

Conclusions

In summary, the thin empty-shell Bi$_2$WO$_6$ hierarchical structure constructed by the ultrathin nanosheets is obtained by means of the acid sculpture effect without any templates or surfactants at a hydrothermal process. The evolved mechanism of the hierarchical thin empty-shell architecture mainly is attributed to the synergistic effect of Ostwald ripening and acid sculpture. Furthermore, it exhibits high specific surface area and abundant pores distribution, which can provide more reactive active sites and molecule transport paths for improving photocatalytic activity. The resulting photodegradation activity for removing coloured RhB and colourless phenol it exhibits is obviously improved compared with the typical Bi$_2$WO$_6$ sample.

Acknowledgements

Notes and references

[a] Department of Chemistry, Harbin Institute of Technology, Harbin 150001, P. R. China. E-mail: gchen@hit.edu.cn; jxsun@hit.edu.cn
[b] School of Municipal and Environmental Engineering, Harbin Institute of Technology, Harbin 150001, P. R. China
[c] Department of Chemistry, Baicheng Normal University, Baicheng 137000, P. R. China

1 O. Legrini, E. Oliveros and A. M. Braun, *Chem. Rev.*,1993, **93**, 671-689.
2 S. W. Liu, J. G. Yu and M. Jaroniec, *J. Am. Chem. Soc.*, 2010, **132**, 11914-11916.
3 K. Shang, B. Sun, J. C. Sun, J. Li and S.Y. Ai, *New J. Chem.*, 2013, **37**, 2509-2514.
4 Y. Yin, R. M. Rioux, C. K. Erdonmez, S. Hughes, G. A. Somorja and A. P. Alivisatos, *Science*, 2004, **304**, 711-714.
5 Z. Q. Li, Y. Ding and Y. J. Xiong, *Chem. Commun.*, 2005, 918-920.
6 J. Hu, M. Chen, X. S. Fang and L. M. Wu, *Chem. Soc. Rev.*, 2011, **40**, 5472-5491.
7 J. X. Zhu, Z. Y. Yin, D. Yang, T. Sun, H. Yu, H. E. Hoster, H. H. Hng, H. Zhang and Q. Y. Yan, *Energy Environ. Sci.*, 2013, **6**, 987-993.
8 J. X. Sun, G. Chen, J. Z. Wu, H. J. Dong and G. H. Xiong, *Appl. Catal. B: Environ.*, 2013, **132-133**, 304-314.
9 N. Zhang, R. Ciriminna, M. Pagliaro and Y. J. Xu, *Chem. Soc. Rev.*, 2014, **43**, 5276-5287.
10 L. S. Zhang, H. L. Wang, Z. G. Chen, P. K. Wong and J. S. Liu, *Appl. Catal. B: Environ.*, 2011, **106**, 1-13.
11 Y. X. Zhou, L. Tong, X. H. Zeng and X. B. Chen, *New J. Chem.*, 2014, **38**, 1973-1979.

12 L. Jiang, L. Z. Wang and J. L. Zhang, *Chem. Commun.*, 2010, **46**, 8067-8069.

13 C. Zhang and Y. F. Zhu, *Chem. Mater.*, 2005, **17**, 3537-3545.

14 Y. Y. Li, J. P. Liu, X. T. Huang and G. Y. Li, *Cryst. Growth Des.*, 2007, **7**, 1350-1355.

15 L. S. Zhang, W. Z. Wang, L. Zhou and H. L. Xu, *Small*, 2007, **3**, 1618-1625.

16 D. Q. He, L. L. Wang, H. Y. Li, T. Y. Yan, D. J. Wang and T. F. Xie, *CrystEngComm*, 2011, **13**, 4053-4059.

17 L.W. Zhang, Y. J. Wang, H. Y. Cheng, W. Q. Yao and Y. F. Zhu, *Adv. Mater.*, 2009, **21**,1286-1290.

18 X. J. Wang, X. L. Wan and L. L. Chang, *Catal. Lett.*, 2014, **144**, 1268-1277.

19 J. G. Yu, H. G. Yu, H. T. Guo, M. Li and S. Mann, *Small*, 2008, **4**, 87-91.

20 X. F. Chen, J. B. Liu, H. Wang, Y. L. Ding, Y. X. Sun and H. Yan, *J. Mater. Chem. A*, 2013, **1**, 877-883.

21 J. G. Yu and J. Zhang, *Dalton Trans.*, 2010, **39**, 5860-5867.

22 H. Cong, Y. Wang, B. Yu, J. Wang and M. Jiao, *New J. Chem.,* 2014, **38**, 2564-2568.

23 X. N. Li, R. K. Huang, Y. H. Hu, Y. J. Chen, W. J. Liu, R. S. Yuan and Z. H. Li, *Inorg. Chem.*, 2012, **51**, 6245-6250.

24 D. X. Wu, H. T. Zhu, C. Y. Zhang and L. Chen, *Chem. Commun.*, 2010, **46**, 7250-7252.

25 H. F. Cheng, B. B. Huang, Y. Y. Liu, Z. Y. Wang, X. Y. Qin, X. Y. Zhang and Y. Dai, *Chem. Commun.*, 2012, **48**, 9729-9731.

26 J. W. Tang, Z. G. Zou and J. H. Ye, *Cata. Lett.*, 2004, **92**, 53-56.

27 Y. Huang, Z. H. Ai, W. K. Ho, M. J. Chen and S. C. Lee, *J. Phys. Chem. C*, 2010, **114**, 6342-6349.

28 M. A. Lovette and M. F. Doherty, *Cryst. Growth Des.*, 2012, **12**, 656-669.

29 Y. Chang, J. J. Teo and H. C. Zeng, *Langmuir*, 2005, **21**, 1074-1079.

30 L. S. Zhang, W. Z. Wang, Z. G. Chen, L. Zhou, H. L. Xu and W. Zhu, *J. Mater. Chem.*, 2007, **17**, 2526-2532.

31 X. X. Yu, J. G. Yu, B. Cheng and B. B. Huang, *Chem. Eur. J.*, 2009, **15**, 6731-6739.

32 R. H. Ouyang, J. X. Liu and W. X. Li, *J. Am. Chem. Soc.*, 2013, **135**, 1760-1771.

33 Y. S. Luo, X. J. Dai, W. D. Zhang, Y. Yang, C. Q. Sun and S. Y. Fu, *Dalton Trans.*, 2010, **39**, 2226-2231.

34 D. J. Wang, L. Guo, Y. Z. Zhen, L. L. Yue, G. L. Xue and F. Fu, *J. Mater. Chem. A*, 2014, **2**, 11716-11727.

35 A. Kudo, I. Tsuji and H. Kato, *Chem. Commun.*, 2002, 1958-1959.

36 N. Tian, H. W. Huang, Y. He, Y. X. Guo and Y. H. Zhang, *RSC Adv.*, 2014, **4**, 42716-42722.

37 H. B. Fu, C. S. Pan, W. Q. Yao and Y. F. Zhu, *J. Phys. Chem. B*, 2005, **109**, 22432-22439.

38 C. M. Li, G. Chen, J. X. Sun, H. J. Dong, Y. Wang and C. D. Lv, *Appl. Catal. B: Environ.*, 2014, **160-161**, 383-389.

39 H. J. Dong, G. Chen, J. X. Sun, C. M. Li, Y. G. Yu and D. H. Chen, *Appl. Catal. B: Environ.*, 2013, **134-135**, 46-54.

40 X. X. Hu and C. Hu, *J. Solid State Chem.*, 2007, **180**, 725-732.

41 H. J. Dong, G. Chen, J. X. Sun, Y. J. Feng, C. M. Li, G. H. Xiong and C. D. Lv, *Dalton Trans.*, 2014, **43**, 7282-7289.

42 L. Ruan, J. Liu, Q. Zhou, J. Hu, G. Xu, X. Shu and Y. Wu, *New J. Chem.*, 2014, **38**, 3022-3028.

43 H. J. Dong, G. Chen, J. X. Sun, Y. J. Feng, C. M. Li and C. D. Lv, *Chem. Commun.*, 2014, **50**, 6596-6599.

44 S. J. Liu, Y. F. Hou, S. L. Zheng, Y. Zhang and Y. Wang, *CrystEngComm*, 2013, **15**, 4124-4130.

45 G. I. N. Waterhouse, G. A. Bowmaker and J. B. Metson, *Phys. Chem. Chem. Phys.*, 2001, **3**, 3838-3845.

46 W. Lin, B. Xu and L. Liu *New J. Chem.*, 2014, **38**, 5509-5514.

47 Z. F. Huang, J. J. Song, L. Pan, F. L. Lv, Q. F. Wang, J. J. Zou, X. W. Zhang and L. Wang, *Chem. Commun.*, 2014, **50**, 10959-10962.

48 C. M. Li, G. Chen, J. X. Sun, Y. J. Feng, J. J. Liu and H. J. Dong, *Appl. Catal. B: Environ.*, *Appl. Catal. B: Environ.*, 2015, **163**, 415-423.

New Journal of Chemistry Accepted Manuscript